Journal of Innovative Optical Health Sciences
Vol. 10, No. 4 (2017) 1740002 (8 pages)

DOI: 10.1142/S1793545817400028

World Scientific
www.worldscientific.com

Optical fluence compensation for handheld photoacoustic probe: An *in vivo* human study case

Lingyi Zhao*, Meng Yang†, Yuxin Jiang† and Changhui Li*,‡
*Department of Biomedical Engineering, College of Engineering
Peking University, Beijing, China
†Department of Ultrasonography, Peking Union Medical College Hospital
Chinese Academy of Medical Sciences & Peking Union Medical College
Beijing 100730, China
‡chli@pku.edu.cn

Received 31 March 2017
Accepted 14 June 2017
Published 20 July 2017

Integrating photoacoustic (PA) and ultrasound (US) into a handheld probe to perform PA/US dual-modal imaging has been widely studied over the past few years. However, optical fluence decreases quickly in deeper tissue due to light scattering and absorption, which would significantly affect the quantitative PA imaging. In this paper, we performed a fluence compensation for a PA imaging study of human breast. The comparison of PA/US image with and without optical fluence compensation demonstrated that the fluence compensation could effectively improve imaging quality for handheld probe.

Keywords: PA imaging; ultrasound; optical fluence.

1. Introduction

According to the American Cancer Society, breast cancer is the most frequently and the second leading cause of cancer death in women in the USA.[1] Although X-ray mammography plays an important role in the detection of breast cancer, it could miss cancers especially in women with dense breasts or lack of microcalcification.[2] In addition, the radiation hazard of X-ray mammography makes it unsuitable for frequent examination. In contrast, ultrasound (US) detection is a safe and routing method, and is capable of visualizing small node-negative breast cancers that are not effectively identified by X-ray mammography.[3] However, US has a relative low specificity, and it highly depends on the experience and skills of the physician.[4]

Photoacoustic (PA) imaging is an emerging hybrid imaging modality, which relies on tissue optical

‡Corresponding author.

properties. It can provide sensitive optical imaging of deep targets with high ultrasonic spatial resolution.[5] In addition, it is noninvasive and safe, which makes it suitable for not only medical screening but also long-term frequent prognosis evaluation. Over the past few years, PA imaging has gained a lot of progresses in both technology development and implementations.[6] Among those progresses, the combination of PA and US with handheld probe has drawn much attention owing to its dual-modality capability.[7–10] Combining a traditional clinical linear probe with optical fiber bundles is a popular method to build the PA/US probe, and this type of probe has been used to image sentinel lymph node,[8,11] human vessels of forearm,[7] human thyroid.[12]

The initial PA pressure is proportional to the product of local optical absorption coefficient and the optical fluence deposited at the same location. However, the optical fluence could vary significantly in living tissue, so the optical fluence compensation is essential for quantitative PA imaging.[13] In this study, we demonstrated our PA/US dual mode imaging result of human breast with and without optical fluence compensation. Our result has shown that light compensation could effectively improve the imaging quality in deeper tissue.

2. Methods and Material

2.1. *System setup*

The dual-modality imaging system was based on a modified high-end commercial clinical US system (Resona7, Mindray Bio-Medical Electronics Co., Ltd., China), which is capable of parallel data acquisition. A clinical 192 elements linear probe with 5.8 MHz-central-frequency (L9-3U, Mindray Bio-Medical Electronics Co., Ltd., China) was used. The system could perform PA imaging on receive-only mode with all US imaging functions preserved. The laser source is a Q-switched Nd:YAG laser (LS-2137/2, LOTIS TII, Minsk, Belarus), which could generate 1064 nm laser pulses at 10 Hz. We also customized a one-two bifurcate optical fiber bundle (made by Nanjing Chunhui Science and technology Industrial Co. Ltd., Nanjing, China) to deliver the laser. Two fiber bundle terminals were mounted on the two sides of the probe, as shown in Fig. 1. To avoid unwanted PA signals caused by light illumination on probe head, a thin film made of

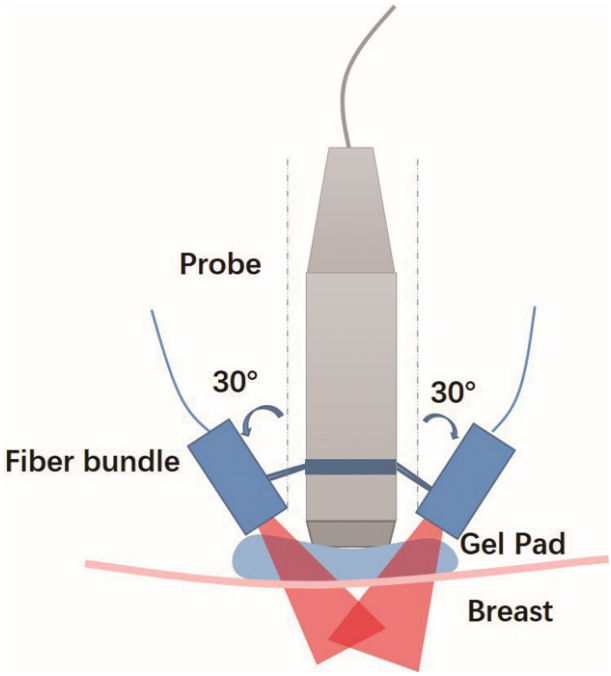

Fig. 1. Schematic diagram of dual-modality imaging setup.

silica gel mixed with TiO_2 particles covered the front surface of the probe.

In addition, a 4 mm-thick transparent soft gel pad was placed between the tissue surface and the probe, and the illumination incident angle of laser was 30°, as shown in Fig. 1.

We performed our PA imaging on a 47 year old woman. The enrollment of the research is approved by the Institutional Ethics Committee of Peking Union Medical College Hospital.

2.2. *Method*

2.2.1. *Theory of fluence compensation*

According to the mechanism of PA effect, within the condition of short laser pulse, the initial PA pressure p_0 can be calculated as follows[14]:

$$p_0(\boldsymbol{r}) = \frac{\beta v_s^2}{C_P} A(\boldsymbol{r}) = \Gamma A(\boldsymbol{r}), \tag{1}$$

where β is the volume thermal expansivity, C_p is the constant-pressure specific-heat capacity, v_s is the sound speed, and A is the absorbed energy density (specific optical absorption) that is transformed into heat at location $\boldsymbol{r}$ per unit volume per laser pulse. Γ is the Grüeneisen coefficient representing the efficiency of the conversion of heat to pressure. If the absorption coefficient at point $\boldsymbol{r}$ is $\mu_a(\boldsymbol{r})$ and the

optical fluence is $F(\boldsymbol{r})$, then $A(\boldsymbol{r})$ can be rewritten as follows:

$$A(\boldsymbol{r}) = \mu(\boldsymbol{r}) \times F(\boldsymbol{r}) \quad \text{and} \quad \mu_a(\boldsymbol{r}) = A(\boldsymbol{r})/F(\boldsymbol{r}). \tag{2}$$

According to Eqs. (1) and Eq. (2), the initial pressure $p_0(\boldsymbol{r})$ is proportional to the product of $\mu_a(\boldsymbol{r})$ and $F(\boldsymbol{r})$. In general, the optical fluence $F(\boldsymbol{r})$ is nonuniform in tissue due to the strong light scattering and absorption. Thus, the reconstructed initial pressure $p_0(\boldsymbol{r})$ could not accurately represent the distribution of absorption coefficient $\mu_a(\boldsymbol{r})$. Therefore, this nonuniform optical fluence might cause the low contrast in deeper tissue where $F(\boldsymbol{r})$ decreased greatly. If the optical parameters of the tissue is known, one can calculate the optical fluence by solving the photon diffusion equation using the finite element method.[15,16] In this study, we imaged the breast tissue structure by US, and then we could set appropriate optical parameters for different types of tissues and solve the optical fluence of tissue. With the known optical fluence distribution, the real optical coefficient can be calculated according to Eq. (2) via dividing the PA reconstruction images by local fluence values.

2.2.2. *Phantom study*

To evaluate the performance of the proposed compensation method, we did a phantom study. In this phantom study, as shown in Fig. 2, we embedded two 0.6 mm diameter carbon rods in two layers of cuboid agar phantom with intra lipid added. The weight concentration of intra lipid (IL) was 3.3% at first layer and 1.8% at second layer. The third layer was pure agar phantom without any IL added. Then we imaged these two carbon rods with both US mode and PA mode. Two black solid lines in Fig. 2(b) represented two carbon rods to be imaged. It should be noted that the top layer of gel pad and the third layer of the phantom were considered as transparent mediums, and they provide two index-matched boundary conditions for the top and bottom boundaries in COMSOL simulation. The illumination incident angle of laser was 45°, as shown in Fig. 2(b).

The reduced optical scattering coefficient of 0.1% IL at wavelength of 1064 nm was measured to be 0.832 cm^{-1}. Thus, in our COMSOL simulation, the reduced optical scattering coefficients of the first and second layers were set 27.5 cm^{-1} and 15.0 cm^{-1}, respectively. The absorption coefficients of both these two layers were set 0.12 cm^{-1}, the same with water[17] because water is the main optical absorption substance at this wavelength.

We performed the proposed method by numerical simulation with COMSOL (COMSOL Inc., Sweden). In the diffuse approximation, the light source was equivalent to two bands lying dz beneath and parallel with the phantom surface, which was calculated as

$$dz = l_t' \times \cos 31°, \tag{3}$$

while $l_t' = 0.19$ cm was the transport mean free path in the first layer. The dimension of each band was

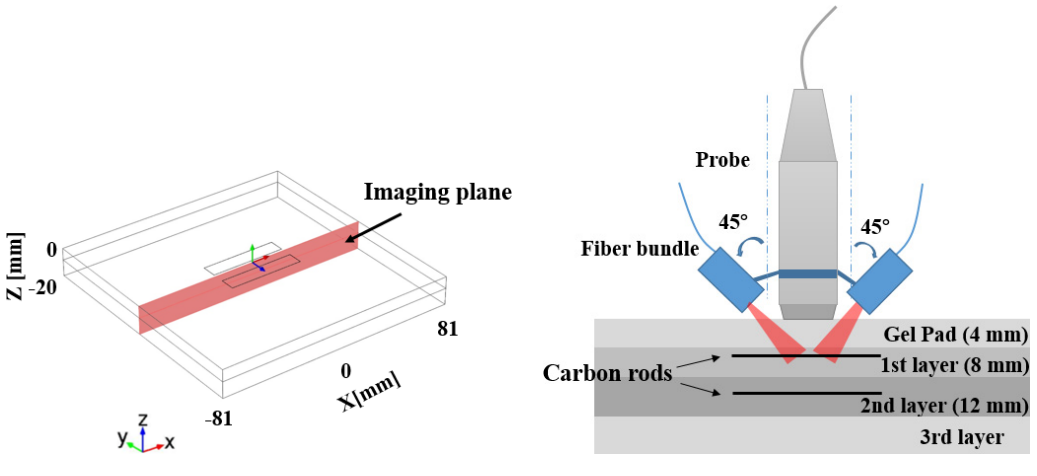

(a) (b)

Fig. 2. (a) The shape of two layers phantom with IL added was assumed to be a cuboid in COMSOL simulation. (b) The schematic diagram of detection setup and three layers.

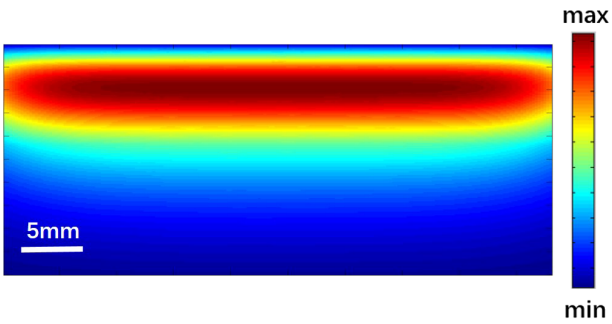

Fig. 3. Φ Map of the central cut plane.

5 cm × 1 cm. Because the refractive index of the gel was similar to that of phantom, the boundary between gel pad layer was treated as a refraction-index-matched one[14]:

$$\Phi(\mathrm{r}) - 2D\nabla\Phi(\boldsymbol{r}) \cdot \boldsymbol{n} = 0, \tag{4}$$

where Φ is the fluence rate (which is proportional to the optical fluence in this study), D is the diffusion coefficient calculated by $D = 1/(3(\mu_a + \mu'_s))$, $\boldsymbol{n}$ is the unit normal vector of the boundary pointing into the phantom layer.

The diffusion equation for global region was given in Eq. (5), and the source condition of two light bands was set to be Eq. (6),

$$-\frac{1}{\mu_{\mathrm{eff}}^2}\nabla^2\Phi + \Phi = 0, \tag{5}$$

$$\frac{1}{\mu_{\mathrm{eff}}^2}\nabla\Phi \cdot \boldsymbol{n} = S, \tag{6}$$

where μ_{eff} is the effective attenuation coefficient calculated by $\mu_{\mathrm{eff}} = \sqrt{\mu_a/D}$, and S is the optical source. Boundary conditions of other four side surfaces of the cuboid were all set to be zero fluence as the distance is large enough for optical fluence to be negligible at these surfaces. The simulation result of optical fluence distribution at imaging plane was shown in Fig. 3.

We carried out our optical fluence compensation by dividing the original reconstructed PA image with the optical fluence map as shown in Fig. 3. Figures 4(a) and Fig. 4(b) showed reconstructed PA image with and without optical fluence compensation, respectively. Both figures were normalized to their maximum value in Fig. 4(a). In addition, the US image was also shown in Fig. 4(c). In Fig. 4(a), the bottom carbon rod at the second layer was almost invisible while in Fig. 4(b) after compensation, it could be seen as clear as the upper carbon rod at first layer.

To evaluate the effect of the compensation method quantitatively, Table 1 compared the normalized values before and after compensation.

Theoretically, absorption coefficients of these two carbon rods were the same and they should give out same value after compensation. As seen in the table, after compensation, the bottom carbon rod clearly shows up, and the corrected PA value of the bottom carbon rod was close to the upper carbon rod. Therefore, this phantom study showed that our optical fluence compensation method in this case was very effective.

2.2.3. *A pilot preclinical study*

In the preclinical case study, we performed the proposed method by numerical simulation with COMSOL (COMSOL Inc., Sweden) as well. In this simulation model, since the probe (∼4 cm long) is much smaller than the breast and the reconstructed region was only up to 2 cm beneath the skin, the breast (shown in Fig. 5(a)) is large enough to be as a semi-infinite medium considering the quick fluence decrease as the distance from the probe. The simulation cuboid has a dimension of

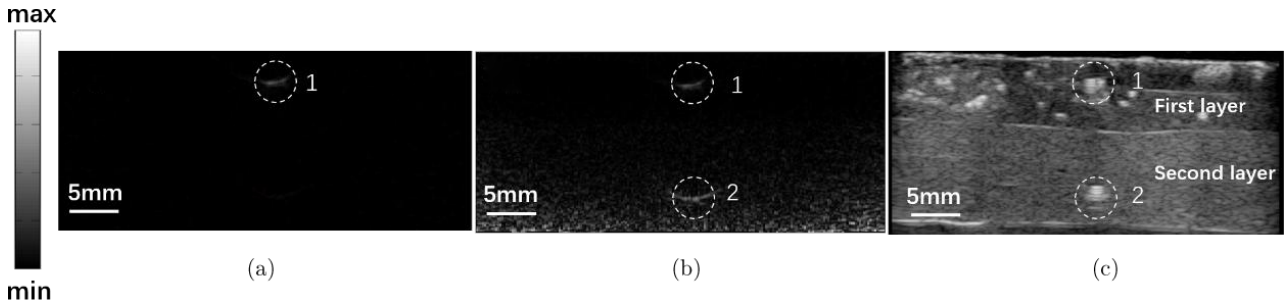

Fig. 4. (a), (b) PA images of phantom with and without optical fluence compensation; (c) US images of the same phantom.

Table 1. Comparison of PA values before and after compensation.

Carbon rod number	Depth (mm)	Before compensation	After compensation
1	3.0	1	1
2	14.5	0.142	1.30

200 mm × 200 mm × 154 mm and consists of three layers: a 4 mm-thick gel layer, a 3 mm-thick skin layer, and a 147 mm-thick breast adipose layer. The schematic diagram of detection for this model was shown in Fig. 5(b), which corresponded to yz plane across $x = 0$ in Fig. 5(a).

The absorption and scattering coefficients of the transparent gel pad layer were all set to be zero. As shown in Fig. 5(b), according to the previous literatures, the absorption coefficient and the reduced scattering coefficient of the skin layer are $\mu_{a_1} = 0.1\,\text{cm}^{-1}$ and $\mu'_{s1} = 10\,\text{cm}^{-1}$,[18] respectively; the absorption coefficient and the reduced scattering coefficient of adipose layer are $\mu_{a_2} = 0.091\,\text{cm}^{-1}$, and $\mu'_{s2} = 6\,\text{cm}^{-1}$,[19] respectively.

The incident angle of laser illuminating on skin surface was 21° (considering the light refraction from air to gel pad). In the diffuse approximation, the light source was equivalent to two bands lying dz beneath and parallel with the skin surface, which was calculated as

$$dz = l'_t * \cos 21°, \tag{7}$$

while $l'_t = 0.1$ cm was the transport mean free path. The dimension of each band was 5 cm × 1 cm.

Because the refractive index of the gel was similar to that of tissue, the boundary between gel pad layer and skin layer was treated as Eq. (4) and $\boldsymbol{n}$ is the unit normal vector of the boundary pointing into the skin layer. The diffusion equation for global region was given in Eq. (5), and the source condition of two light bands was set to be Eq. (6). Boundary conditions of other five surfaces of the cuboid were set to be zero fluence as the distance is large enough for optical fluence to be negligible at these surfaces. The cuboid was meshed into free tetrahedral with element size of extra fine defined by COMSOL, 1012184 elements in total. Then COMSOL was used to solve the optical fluence of the cuboid. The calculated optical fluence in the central cut plane was shown in Fig. 6(a), which was used as the relative compensation coefficient map to be applied to compensate the the PA images

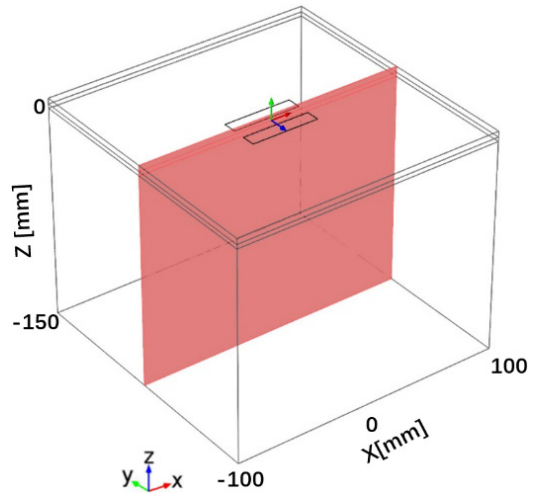

(a)

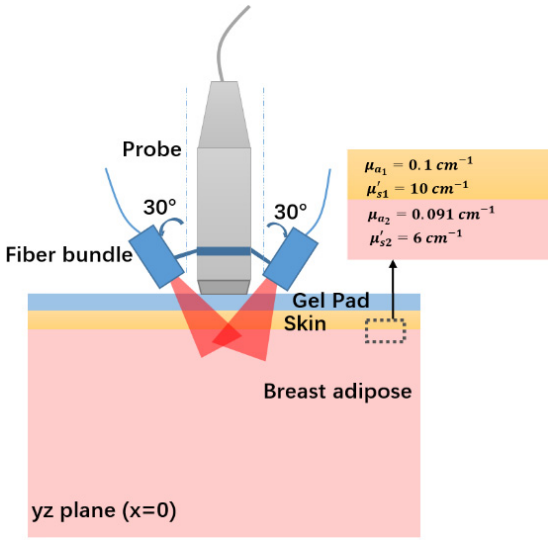

(b)

Fig. 5. (a) The shape of breast tissue was assumed to be a cuboid and (b) the schematic diagram of detection setup.

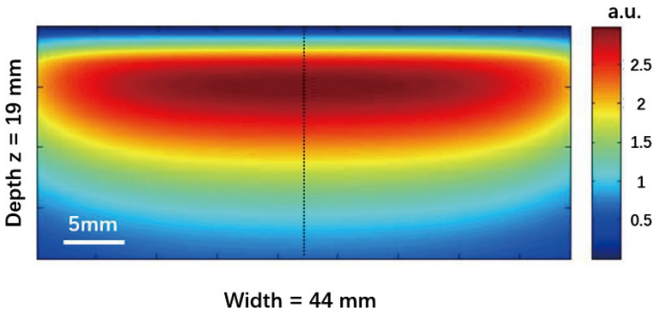

(a)

Fig. 6. (a) Relative Φ map of the central cut plane. (b) Relative fluence along the dark dotted line.

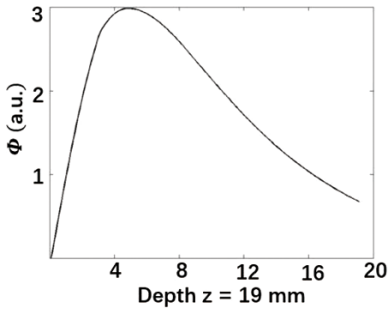

(b)

Fig. 6. (*Continued*)

according to Eq. (2). The fluence variance along the centerline (as marked dashed in Fig. 6(a)) was plotted in Fig. 6(b).

3. Results of Preclinical Study Case

Figure 7(a) showed the original reconstructed PA image (based on the delay and sum algorithm). The primary PA sources under skin are vessels. We marked four vessels (white dashed circles) values at different depths. As discussed before, the reconstructed values become weaker as the depth increases, and the No. 4 vessel becomes almost invisible. By dividing Fig. 7(a) with the fluence map in Fig. 6(a), the optical fluence compensation was applied to original PA reconstruction images as shown in Fig. 7(b). Both Figs. 7(a) and 7(b) were normalized to their maximum values.

Table 2. Comparison of PA values before and after compensation.

Vessel number	Depth (mm)	Before compensation	After compensation	Relative fluence
1	3.0	1	1	2.7379
2	7.3	0.8386	0.8971	2.5749
3	9.6	0.3428	0.4300	2.1830
4	14.4	0.1172	0.2908	1.1031

To demonstrate the compensation effect quantitatively, Table 2 compared their normalized values before and after compensation.

As seen in the table, reconstructed vessel values in deeper region were significantly increased (more than two fold). Therefore, the No. 4 vessel becomes much more prominent as shown in Fig. 7(b).

To construct a fused US/PA image, people generally set a threshold for PA image. In this study, we set 15% of the maximum value as the threshold. Figure 8 showed the comparison of before and after optical fluence compensation for fused images.

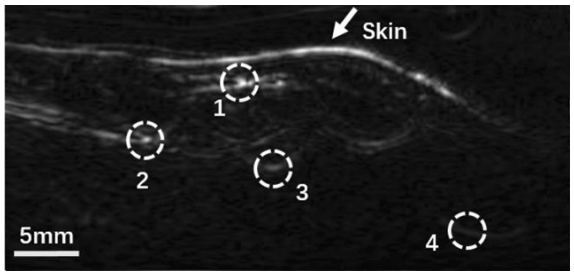

(a)

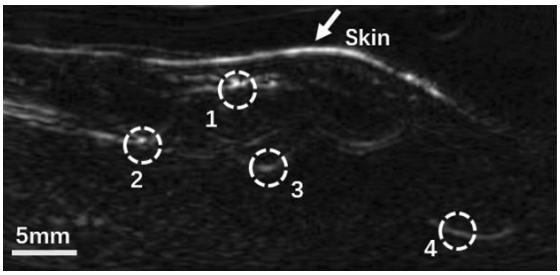

(b)

Fig. 7. (a) PA image of breast without optical fluence compensation. (b) PA image of breast with optical fluence compensation.

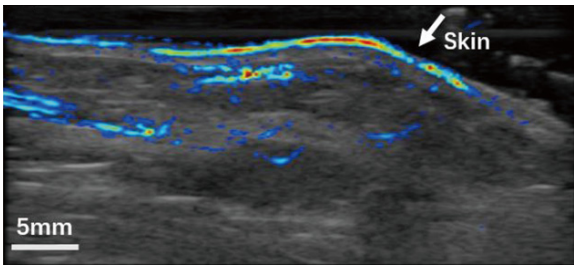

(a)

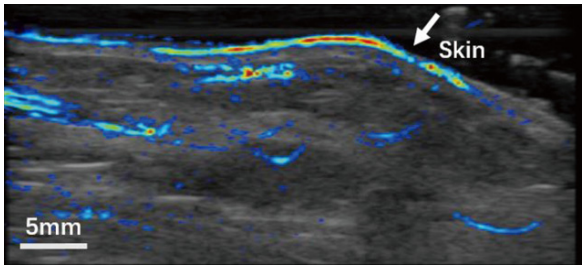

(b)

Fig. 8. (a) US/PA dual mode image without compensation of optical fluence. (b) US/PA dual mode image with compensation of optical fluence.

Without compensation, vessels with weak signal might be missed in the fused PA/US image (as the No. 4 vessel in the right bottom location). However, optical fluence compensation also caused the increase in background signal, including noise in deeper region, leading to a lower signal to noise ratio. For instance, besides the No. 4 vessel, another new pattern also shows up in the left bottom of Fig. 8(b), which is suspected to be the amplified noise signal.

4. Discussion

In this study, based on an *in vivo* human study, we showed that optical fluence compensation could be important for handheld PA/US probe. We calculated optical fluence using finite element method by COMSOL, and the computation results can effectively compensate the fluence drop effect. Although some researchers also used Monte Carlo method to perform similar progress,[20] it needs much longer calculation time and is not suitable for future real-time processing.

However, the simple simulation model used in this work is still far from the real condition. The structure of breast tissue was not a simplified sandwiched pattern, and it will have much more complicated three-dimensional structures. In the future, we will acquire 3D breast anatomical imaging to achieve realistic breast tissue components and morphology, and then we can set different optical parameters into the model to solve the equation. Besides, this optical fluence compensation method could cause serious decrease of SNR in the deeper region. A more sensitive probe for PA imaging is also desired to suppress the noise level.

In conclusion, our study showed that with optical fluence compensation, we could regain important information of PA/US images in deeper tissue. It is essential for future clinical studies for quantitative PA/US imaging, which aims at the diagnosis of breast tumor based on vascular morphology and functional information (like oxygen saturation).

Acknowledgments

This research was founded by International S&T Cooperation Program of China (2015DFA30440), National Natural Science Foundation of China (81301268, 81421004), Beijing Nova Program (Z131107000413063), and The National Key Instrumentation Development Project (2013YQ030651)

References

1. R. Siegel, D. Naishadham, A. Jemal, "Cancer statistics, 2013," *Ca Cancer J Clin.* **63**, 10–29 (2013).
2. H. D. Cheng, X. Cai, X. Chen, L. Hu, X. Lou, "Computer-aided detection and classification of microcalcifications in mammograms: A survey," *Pattern Recognit.* **36**, 2967–2991 (2003).
3. W. A. Berg, J. D. Blume, J. B. Cormack, E. B. Mendelson, D. Lehrer, M. Bohm-Velez, E. D. Pisano, R. A. Jong, W. P. Evans, M. J. Morton, "Combined screening with ultrasound and mammography vs mammography alone in women at elevated risk of breast cancer," *Jama* **299**, 2151–2163 (2008).
4. W. Teh, A. R. Wilson, "The role of ultrasound in breast cancer screening. A consensus statement by the European Group for Breast Cancer Screening," *Eur. J. Cancer* **34**, 449–450 (1998).
5. C. Li, L. V. Wang, "Photoacoustic tomography and sensing in biomedicine," *Phys. Med. Biol.* **54**, R59–R97 (2009).
6. L. V. Wang, S. Hu, "Photoacoustic tomography: In vivo imaging from organelles to organs," *Science* **335**, 1458–1462 (2012).
7. M. P. Fronheiser, S. A. Ermilov, H.-P. Brecht, A. Conjusteau, R. Su, K. Mehta, A. A. Oraevsky, "Real-time optoacoustic monitoring and three-dimensional mapping of a human arm vasculature," *J. Biomed. Opt.* **15**, 021305–021307 (2010).
8. C. Kim, T. N. Erpelding, L. Jankovic, M. D. Pashley, L. V. Wang, "Deeply penetrating in vivo photoacoustic imaging using a clinical ultrasound array system," *Biomed. Opt. Express* **1**, 278–284 (2010).
9. A. Taruttis, A. C. Timmermans, P. C. Wouters, M. Kacprowicz, G. M. V. Dam, V. Ntziachristos, "Optoacoustic imaging of human vasculature: Feasibility by using a handheld probe," *Radiology* **281**, 256–263 (2016).
10. D. Yang, D. Xing, Y. Tan, H. Gu, S. Yang, "Integrative prototype B-scan photoacoustic tomography system based on a novel hybridized scanning head," *Appl. Phys. Lett.* **88**, 817 (2006).
11. A. Garcia-Uribe, T. N. Erpelding, A. Krumholz, H. Ke, K. Maslov, C. Appleton, J. A. Margenthaler, L. V. Wang, "Dual-modality photoacoustic and ultrasound imaging system for noninvasive sentinel lymph node detection in patients with breast cancer," *Sci. Rep.* **5**, 15748 (2015).
12. J. Kim, M. H. Kim, K. Jo, J. Ha, Y. Kim, D. J. Lim, C. Kim, "Photoacoustic analysis of thyroid cancer in vivo: A pilot study," *Proc. SPIE* (2017), 1006408.
13. Z. Yuan, H. B. Jiang, "Quantitative photoacoustic tomography: Recovery of optical absorption coefficient maps of heterogeneous media," *Appl. Phys. Lett.* **88**, 231101–231103 (2006).

14. L. V. Wang, H. I. Wu, *Biomedical Optics: Principles and Imaging* (John Wiley & Sons, 2012).
15. S. R. Arridge, "Optical tomography in medical imaging," *Inverse Probl.* **15**, R41 (1999).
16. K. D. Paulsen, H. Jiang, "Spatially varying optical property reconstruction using a finite element diffusion equation approximation," *Med. Phys.* **22**, 691–701 (1995).
17. G. M. Hale, M. R. Querry, "Optical constants of water in the 200-nm to 200-μm wavelength region," *Appl. Opt.* **12**, 555–563 (1973).
18. J. L. Sandell, T. C. Zhu, "A review of *in-vivo* optical properties of human tissues and its impact on PDT," *J. Biophotonics* **4**, 773–787 (2011).
19. V. Peters, D. Wyman, M. Patterson, G. Frank, "Optical properties of normal and diseased human breast tissues in the visible and near infrared," *Phys. Med. Biol.* **35**, 1317 (1990).
20. S. Bu, Z. Liu, T. Shiina, K. Kondo, M. Yamakawa, K. Fukutani, Y. Someda, Y. Asao, "Model-based reconstruction integrated with fluence compensation for photoacoustic tomography," *IEEE Trans. Biomed. Eng.* **59**, 1354–1363 (2012).